A model of silica colloid growth, stability and transport used to predict geothermal reinjection lifetime

Shuying Chen[1], Kevin Brown[2], and Mark Jermy[1]

[1] Department of Mechanical Engineering, University of Canterbury, Christchurch 8041, New Zealand

[2] GEOKEM, P.O. Box 30-125, Barrington, Christchurch, New Zealand

jasonchen1212@hotmail.com

Keywords: *injectivity, silica scaling, amorphous silica deposition, geothermal reinjection, silica polymerization, colloidal silica stability.*

ABSTRACT

When cooled geothermal brine is reinjected, deposited silica may block the fluid pathways in the aquifer, reducing injectivity. Previous authors have used TOUGHREACT to successfully model silica deposition, using an empirically determined reaction rate to predict the rate of deposition. An a-priori model of hydrodynamic effects on the transport of colloidal silica is desirable. This paper describes a new model of fluid flow and silica particle nucleation, growth and transport. 1D transport PDEs are solved for heat and mass transfer. Silica particle growth is modelled by considering homogeneous nucleation and growth due to molecular deposition (Weres et al. 1981), Ostwald ripening (Wagner 1961), and aggregation (Elimelech et al. 2013, Škvarla 2013).

The deposition rate is sensitive to the stability (resistance to aggregation) of the colloidal particles. DLVO theory predicts stabilities which, under certain conditions, differ from experimental observations. The model implements empirical stability relationships fitted to experimental data. The model replicates bench observations of silica growth and stability (Weres et al. 1981, Škvarla 2013, Tobler and Benning 2013). It is used to model deposition in the fracture networks of a simplified geothermal reservoir. The results are compared to the injectivity predictions of Xu et al. (2004).

1. INTRODUCTION

To maintain reservoir pressure and sequester toxic minerals, condensed geothermal brine is often reinjected into the aquifer. The decrease in amorphous silica solubility due to cooling and loss of steam may cause deposition of silica which blocks the fluid pathways near the reinjection well.

Commercial packages like TOUGHREACT (Xu 2008) have been used to understand this numerically (Xu et al. 2004, Wong et al. 2016), using an empirical reaction rate to predict the deposition rate. This can be accurate, but the empirical reaction rate must be estimated for each new set of conditions. A model that predicts it a priori is desired.

2. METHODOLOGY

2.1 Problem set up

The injectivity index (Eq. 1), II (t hr^{-1} bar^{-1}) quantifies the ease of reinjection.

$$II = \frac{Mass\ flow\ rate}{P_{inj} - P_{res}} \quad (1)$$

where P_{inj} is the pressure of the injected fluid and P_{res} is the initial pressure of the reservoir. If silica deposition can be predicted, so can the decline of injectivity, the lifetime of the reinjection well, and the effect of chemical workover. The structure of the present model is outlined in Fig. 1.

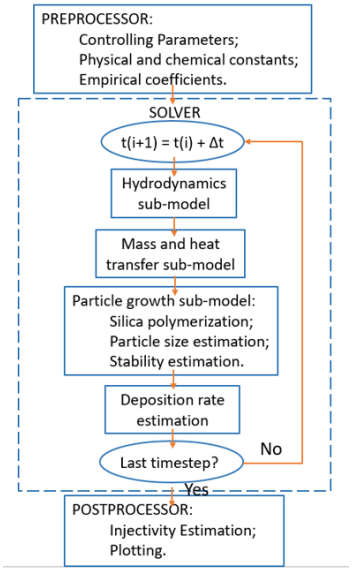

Figure 1: Workflow of the model.

This holistic model couples sub-models of fluid mechanics, thermodynamics, silica and calcite chemistry, and colloid transport. Partial differential equations are solved with the Finite Volume method (FVM) to ensure conservation of mass and energy.

2.1.1 Geometry set up

The cooled geothermal fluid is reinjected through the wellbore (Fig. 2, blue cylinder) and is assumed to only spread along horizontal fracture networks, which are homogeneously distributed in the vertical direction. The geometry is thus axis-symmetric with radial distance from the wellbore represented by R. The reservoir is assumed vertically homogenous, i.e. rock properties are constant over a certain range of depths between impermeable basement and cap rocks. The model is clearly much simpler than real geothermal reservoirs, but serves to demonstrate the evolution of the silica.

It is assumed that the sub-horizontal fractures are the preferential flow paths, though they may account for a relatively small part of the whole porosity. Since the radial distance R is bigger than the fracture aperture a by several orders of magnitude, the fracture network is treated as equivalent to pairs of parallel flat plates (Figure 3).

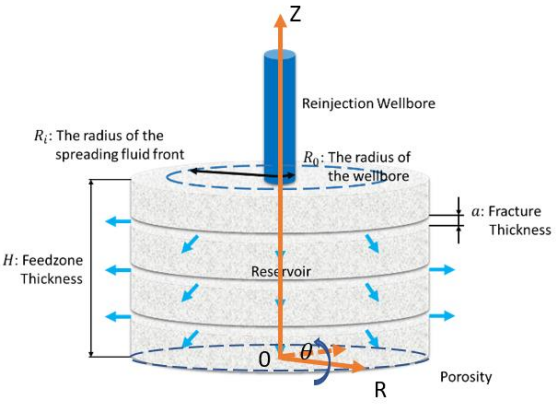

Figure 2: Simplified geometry consisting of injection wellbore and geothermal reservoir.

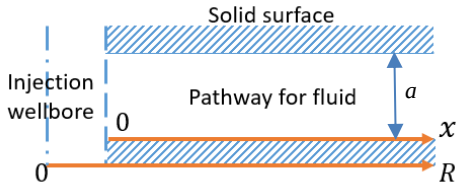

Figure 3: Parallel flat plate model showing the radial distance R and the (fluid) spreading distance $x = R - R_0$.

2.1.2 Computational Mesh

Time and space are separately discretized by a timestep dt and spatial cell size dx (equal to the increment in radius between adjacent cells).

To express the time and spreading distance along the sub-horizontal fractures, the following parameters are defined:

$$x_i = (i-1)dx, \quad 0 < i < N_i = \frac{x_{max}}{dx} \tag{2}$$

$$t_j = (j-1)dt, \quad 0 < j < N_j = \frac{t_{max}}{dt} \tag{3}$$

The subscript "i, j" will be used to indicate the value of interest at the ith cell and the jth timestep.

2.2 Controlling parameters and inputs

The controlling parameters and typical values used for preliminary computations are summarised in Table 1. The values below are reproduced from (Xu et al. 2004), where injectivity drop is reported at Tiwi field, Philippines. The unreported or invalid data are highlighted and replaced with typical NZ-based or assumed values.

Table 1: Summary of input parameters

Notation	Value used	Explanation	Notation	Value used	Explanation
t_{max}	12 year	Time after injection begins	pH_{inj}	4.5	Initial pH of injected fluid[a, b]
R_0	0.122 m	Radius of injection wellbore	pH_{res}	7	Initial pH of reservoir fluid[b]
H	120 m	Thickness of feedzone	I_{inj}	0.07 mol/kg	Initial ionic strength of injected fluid[c]
a_0	0.002 m	Initial fracture aperture	I_{res}	0.09 mol/kg	Initial ionic strength of reservoir fluid[c]
ϕ_0^r	0.01	Initial reservoir porosity	c_{inj}^{SiO2}	1200 ppm	Initial concentration of monomeric silica in injected fluid[d]
ϕ_0^f	1	Initial fracture porosity	c_{res}^{SiO2}	620 ppm	Initial concentration of monomeric silica in reservoir fluid
k_0^f	5.0 $\times 10^{-12}$ m^2	Initial permeability of fractures	c_{inj}^{cp}	0 ppm	Initial concentration of polymerised silica in injected fluid[e]
$\dot{m}$	60 kg/s	Injecting mass flow rate	c_{res}^{cp}	0 ppm	Initial concentration of polymerised silica in reservoir fluid[e]
T_{inj}	160 ℃	Initial temperature of injected fluid	q	4	Power exponent of Equation 31
T_{res}	260 ℃	Initial temperature of reservoir			

a: pH_{inj} = 4.5 is used to unravel the negligible effects of acidification on silica scaling underground; b: equivalent pH at the room temperature; c: sodium chloride is assumed to be the only electrolyte in the injected brine; d: c_{inj}^{SiO2} is originally reported to be 705 – 710 ppm at 160 ℃ under unknown pH and ionic strength, which is out of the regime of homogenous nucleation of colloidal silica and interest; e: it is assumed that before the reinjection there is no polymerised silica at all in either injected or reservoir fluid.

2.3 Sub-models

The solver consists of several sub-models. Partial differential equations are solved with the QUICK scheme (Leonard 1979).

2.3.1 Hydrodynamics model

This model is used to find the velocity at which the fluid travels away from the wellbore, within the fractures. As the density of water changes little (decreasing by approximately 13% on heating from 155 ℃ to 260 ℃ (Keenan 1969)), it is assumed that the fluid is incompressible. Hence, the mass continuity equation can be simplified to Eq. 4:

$$\nabla \cdot \mathbf{u} = 0 \tag{4}$$

Therefore, at time t_i, in each control volume dV:

$$dV = \dot{V}dt = \frac{\dot{m}}{\rho}dt = u_{i,j}A_{i,j}dt \tag{5}$$

where, $\dot{V}$ is the volumetric flow rate, ρ is the density of the injected fluid, $u_{i,j}$ is the fluid spreading velocity, and $A_{i,j}$ is the mean cross-section area of the ith cell, defined by Eq. 6:

$$A_{i,j} = 2\pi[(i-1)dx + \frac{dx}{2}]\mathrm{H}\phi_0^r\phi_{i,j}^f \quad (6)$$

where, $\phi_{i,j}^f$ is the porosity of the fracture, defined by:

$$\phi_{i,j}^f = \frac{a_{i,j}}{a_0} \quad (7)$$

$$a_{i,j} = a_{i,j-1} - 2k_{dep}dt \quad (8)$$

where, k_{dep} is the amorphous silica deposition rate in m/s, defined by the ratio of deposition mass flux j_{dep} and the density of amorphous silica. $j_{dep} = 0$ at t = 0, after which j_{dep} is) computed by the deposition model.

For parallel flat plates the Reynolds number $Re_{i,j}$ is (9):

$$Re_{i,j} = \frac{2u_{i,j}a_{i,j}}{\upsilon} \quad (9)$$

where, υ is the kinematic viscosity of the fluid. By comparing $Re_{i,j}$ to the critical Reynolds number $Re_{crit} = 1400$, the flow regime in the fracture can be predicted. The present results show the flow to be laminar all along the fracture.

2.3.2 Heat transfer model

The governing equation for the transient convection-diffusion heat and mass transfer is:

$$\frac{\partial(\rho\Phi)}{\partial t} + \nabla\cdot(\rho\boldsymbol{u}\Phi) = \nabla\cdot\Gamma\nabla\Phi + S \quad (10)$$

where, Φ represents a property like temperature or species concentration, Γ is the diffusion coefficient, and S is the source term.

In this case, as the fluid is assumed to spread only horizontally, $\frac{\partial\Phi}{\partial\theta}$ and $\frac{\partial\Phi}{\partial z}$ are zero. Therefore, Eq. 10 can be simplified to:

$$\frac{\partial(\rho\Phi)}{\partial t} + \frac{1}{R}\frac{\partial(R\rho\Phi u)}{\partial R} = \frac{1}{R}\frac{\partial}{\partial R}\Gamma R\frac{\partial\Phi}{\partial R} + S \quad (11)$$

Substituting T=Φ, the governing equation for heat transfer is obtained:

$$\rho c\frac{\partial T}{\partial t} + \frac{\rho c}{R}\frac{\partial(RTu)}{\partial R} = \frac{1}{R}\frac{\partial}{\partial R}kR\frac{\partial T}{\partial R} + S \quad (12)$$

where c and k are the heat capacity and the thermal conductivity of the fluid respectively, which are assumed to be fixed and equal to those of water.

Heat transfer occurs between cooled and reservoir fluid, and also between fluid and rock. Eq. 11 is coupled with two set of parameters, inputs, and boundary conditions: one for fluid and the other for rock. The source terms are equal in magnitude and opposite in sign $S_{fluid} = -S_{rock} = \dot{Q}$.

The convective heat transfer between fluid and rock is defined by:

$$\dot{Q} = hA_i^r(T_{rock} - T_{fluid}) \quad (13)$$

where $\dot{Q}$ is the heat flux, $h = \frac{\mathrm{Nu}\,k}{2a_{i,j}}$ is the heat transfer coefficient and Nu is Nusselt number (=7.54 in laminar flow between parallel flat plates), $A_i^r = 2\pi[(idx + R_0)^2 - ((i-1)dx + R_0)^2]$ is the area of the heat transfer surfaces of the *i*th cell, i.e. the area of the top and bottom walls.

The boundary conditions are: $T|_{x=0} = T_{inj}$ and $T|_{x=xmax} = T_{res}$ for fluid, and $T|_{x=0} = T_{inj}$ and $T|_{x=xmax} = T_{res}$ for rock, since $x = 0$ represents the surface of the injection wellbore and x_{max} stands for the far regions of the reservoir.

2.3.3 Mass transfer model

Substituting $C = \rho\Phi$ into Eq. 10, the mass transfer governing equation is obtained:

$$\frac{\partial C}{\partial t} + \frac{1}{R}\frac{\partial(RCu)}{\partial R} = \frac{1}{R}\frac{\partial}{\partial R}DR\frac{\partial C}{\partial R} + S \quad (14)$$

where C represents the concentration of a species of interest: the hydrogen ion, sodium ion (for ionic strength), monomeric silica, or polymerised silica. Hence, four sets of diffusion coefficients D, boundary conditions and source term S are required.

The diffusion coefficient for ions (H^+ and Na^+) is calculated from the Nernst formula:

$$D = \frac{RT\lambda}{|z|F^2} \quad (15)$$

where, R is gas constant, λ is the conductivity, z is the valence of the ion, and F is the Faraday constant.

The diffusion coefficient for colloidal particles (assumed to be spherical) is given by the Stokes-Einstein equation:

$$D = \frac{k_BT}{6\pi\mu r} \quad (16)$$

where, k_B is Boltzmann's constant, μ is the dynamic viscosity of the fluid, and r is the radius of the particle.

The boundary conditions are set up as follows: $C|_{x=0} = 10^{-pHinj}$ and $C|_{x=xmax} = 10^{-pHres}$ for hydrogen ion, $C|_{x=0} = c_{inj}^{Na+} = I_{inj}$ and $C|_{x=xmax} = c_{res}^{Na+} = I_{res}$ for sodium ion, $C|_{x=0} = c_{inj}^{SiO2}$ and $C|_{x=xmax} = c_{res}^{SiO2}$ for monomeric silica, and $C|_{x=0} = c_{inj}^{cp}$ and $C|_{x=xmax} = c_{res}^{cp}$ for polymerised silica.

In the kinetics of calcite dissolution, the dominant factors are temperature and pH. The ionic strength of geothermal fluid is relatively low and the effects of sodium chloride are neglected. According to (Plummer et al. 1978, Arvidson et al. 2003), the calcite dissolution rate constant R^{Ca} can be defined by:

$$R^{Ca} = Ac_{H+}^p exp(-E/k_BT) \quad (17)$$

where A is the pre-exponential factor, p is the power law component, and E is the experimental activation energy. For the sake of simplicity, p may be assumed to be 1. Therefore, Eq. 17 can be rearranged in the form of:

$$\ln R_{i,j}^{Ca} = \mathrm{m}\ln\left(c_{i,j}^{H+}\right) + \frac{\mathrm{n}}{\mathrm{T}_{i,j}} \quad (18)$$

where m and n are empirical constants. There is a lack of observed data at high temperature. Fitting observed datasets made at different pH (i.e. concentration of hydrogen ions) and same temperature (298K) (Figure 4), an empirical expression dependent on $c_{i,j}^{H+}$ at $\mathrm{T}_{i,j} = 298\ K$ may be found, thus the empirical constants m and n can be found.

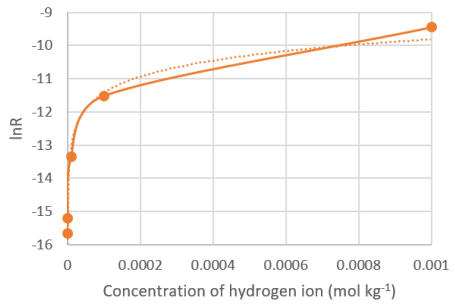

Figure 4: Observed calcite dissolution rate at room temperature. The points are the observations of (Arvidson et al. 2003), the dotted curve is the fitted expression: $\ln R = 0.5629\ln\left(c_{i,j}^{H+}\right) - 7.638$

The fitted curve used in the present case is:

$$\ln R_{i,j}^{Ca} = 0.5629\ln\left(c_{i,j}^{H+}\right) + \frac{2276.124}{\mathrm{T}_{i,j}} \quad (19)$$

And the source term for hydrogen ion transport is:

$$S = -\frac{R_{i,j}A_i^r}{\rho dV} = -\frac{R_{i,j}^{Ca}}{\rho a_{i,j}} \quad (20)$$

For the transport of sodium ions, it is assumed that there are no reactions consuming sodium chloride, and the source term is:

$$S = 0 \quad (21)$$

The source terms for the transport of monomeric and polymerised silica are given in the next section.

2.3.4 Homogenous nucleation model

The kinetics of silica polymerisation in this model follows (Weres et al. 1981). The nucleation rate is defined by:

$$I_N = Q_{LP}ZR_{md}\rho_n A^*\exp(-\Delta F^*/k_BT) \quad (22)$$

where, $Q_{LP} = 3.34\times10^{25}kg^{-1}H_2O$ is Lothe-Pound factor, Z is Zeldovich factor representing the possibility of polymerised silica with critical nucleation size r_{crit} to form nucleus and continue to grow, R_{md} is the molecular deposition rate, ρ_n is the number density of SiO_2 units in solid phase, A^* is the surface area critical nucleus, and ΔF^* is the free energy barrier.

To maintain dimensional consistency, the expression offered in (Weres et al. 1981) was modified to give Eq. 23:

$$I_N = \frac{Q_{LP}\rho ZR_{md}\rho_n A^*}{\rho_{siO2}}\exp(-\Delta F^*/k_BT) \quad (23)$$

where ρ_{siO2} is the density of amorphous silica.

Since the temperature, pH, ionic strength, and concentration of monomeric silica are known, the decrement rate in a certain cell, i.e. the source term for monomeric silica transport, can be expressed by:

$$S = -\frac{R_{md}}{A_{total}} \quad (24)$$

where, A_{total} is the total surface area of the colloidal silica.

An induction time t_{in} is also included, defined as the time needed for an initial noticeable monomeric silica concentration drop (by usually 50 ppm):

$$t_{in} = 1.08\times10^6 R_{md}^{-1}\left(ZQ_{LP}r_{crit}^2\exp\left(-\frac{\Delta F^*}{k_BT}\right)\right)^{1/4} \quad (25)$$

The units of t_{in}, R_{md}, and r_{crit} used in the equation above are min, $gSiO_2cm^{-2}min^{-1}$, and cm, respectively. Other parameters are in SI units.

2.3.5 Particle growth model

Under geothermal conditions, homogeneous nucleation is considered to be the dominant mechanism of initial particle formation (Weres et al. 1981), and molecular deposition of monomeric silica to the particle surface will also be taken into account. At later times, Ostwald ripening and aggregation are the main mechanisms of particle growth.

An in-situ particle size measurement experiment (Tobler and Benning 2013) showed that the size of colloidal silica appearing at the beginning is very close to the critical nucleation size and rapidly grows and then converges to a certain definite size, which is relatively independent of concentration of silica and dependent on temperature and time.

According to (Nielsen 1964), it can be argued that the average particle size is approximately equal to the critical nucleation size when Ostwald ripening dominates the particle growth. However, observations show a large discrepancy from this theory (Figure 5).

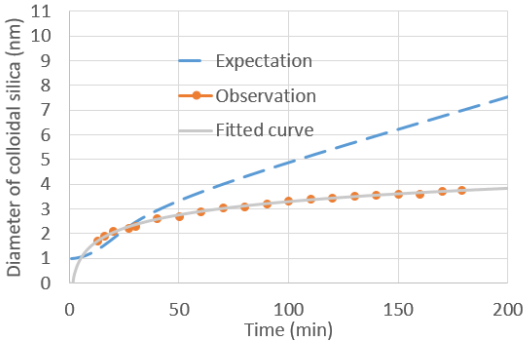

Figure 5: Particle size comparison between observation (dots) and estimation based on Nielsen's theory (dashed curve), and particle size comparison between observation (dots) and fitting result (solid curve): $d = 0.7758\,ln(t) - 0.2848$ (303K, initial dissolved silica concentration: 960ppm, pH=7, ionic strength = 0.03M)

Since the particle size at time t, which is of more interest in this study than the growth rate in the first hour due to the timescale (~years), particle size is considered to be a function of only temperature and time. The initial critical nucleation size predictions are reliable. Thus, an empirical expression for particle estimation is proposed as:

$$d = \varphi\, ln(t) + \omega \tag{26}$$

where, d is the diameter of the particle in nanometres, φ and ω are fitting constants, and t is the time in minutes allowing the particle to grow. This expression is fitted to the data shown in Figure 5.

It is reported (Alexander and McWhorter 1958) that a particle size of 15nm is observed at around 3hr when the temperature is 160℃, which is very close to the conditions in the present model. Therefore, the following expression is fitted by using the data r_{crit} at dt and 15nm at 3 hours and applied to predict the particle growth:

$$d = 2.4921\, ln(t) + 1.7813 \tag{27}$$

2.3.6 Stability model

The stability of colloidal silica W plays a key role of predicting the deposition rate in this study. It is defined by:

$$W = \frac{k_{fast}}{k_{slow}} \tag{28}$$

where, k_{fast} is the diffusion limited, or "fast" aggregation rate constant (only attractive forces present), k_{slow} is the reaction limited (both attractive and repulsive forces present), or "slow" aggregation rate constant. Physically, W represents the stability of a colloidal suspension under the conditions of interest, thus the reciprocal of the observed stability of colloidal silica is the probability of attachment between suspended and deposited particles and may be used to predict the deposition rate.

The DLVO theory (Derjaguin and Landau 1941, Verwey and Overbeek 1955) quantitatively describes the interaction potentials between colloids V_T, which combines both the attraction potential V_A due to the van der Waals force and the repulsion potential V_E due to the electrostatic force:

$$V_T = V_A + V_E \tag{33}$$

The DLVO theory has been used to predict stability of a colloidal suspension and has proved to be reasonably accurate. However, discrepancies up to 20 orders of magnitude between the observed behaviour of colloidal silica and the predictions of the DLVO theory are observed (Škvarla 2013) for silica particles over certain ranges of pH and ionic strength. This discrepancy may lead to underestimation of the deposition rate by orders of magnitude, and serious errors in the predicted lifetime of the reinjection well.

In place of DLVO predictions, an empirical expression fitted to the observations of (Škvarla 2013) is applied:

$$logW = 123.74 d^{-0.904} \tag{29}$$

The expression above is fitted to experimental data for the conditions (298K, pH=6, I=0.07M, and atmospheric pressure) most closely approaching reservoir conditions, among all available reported results. Temperature is the most important parameter as pH increases rapidly to neutral (Figure 7), the ionic strength of the injected fluid does not vary much (Figure 8), and pressure may have limited effects on stability. The lack of stability data at geothermal temperatures requires the coarse assumption that the stability is the same as at 298K.

Given the stability, the aggregation rate constant can be found, therefore the particle size change at time t can be estimated.

2.3.7 Deposition model

A simplified method proposed by Frank-Kamenetskii (Frank-Kamenetskii 1969) is applied to predict the deposition rate. All reaction surfaces are assumed to be equally available for deposition due to diffusion. The deposition mass flux $j_{dep}^{i,j}$ can be expressed as:

$$j_{i,j}^{dep} = \frac{\beta_{i,j} n_{i,j}^{dep}}{n_{i,j}^{dep} + \beta_{i,j}} c_{i,j}^{CP} \tag{30}$$

where, $\beta_{i,j} = \frac{\mathrm{Sh}\, D}{2a_{i,j}}$ is the mass transfer coefficient, Sh=7.54 (for laminar flow) is the Sherwood number, (the ratio of convective mass transfer rate to diffusive mass transfer rate), $n_{dep} = \frac{1}{\mathrm{W}}\sqrt{\frac{D}{2\mathrm{t}}}$ is the effective reaction rate, D is the mass diffusivity of the silica particles, tis the unit time allowing the number of n_{dep} particles that are at a short enough distance to attach to the deposited ones due to diffusion, and $c_{i,j}^{CP}$ is the bulk concentration of polymerised silica.

Only diffusive transport is considered: turbulent transport and inertial impaction onto irregularities in the fractures is neglected in the present case.

2.3.8 Computation of injectivity

Accumulating the deposition over time gives the change in fracture porosity directly. The correlation between porosity and permeability is suggested by (Verma and Pruess 1988) :

$$\frac{k_{i,j}^f}{k_0^f} = \left(\frac{\emptyset_{i,j}^f - \emptyset_c^f}{\emptyset_0^f - \emptyset_c^f}\right)^q \tag{31}$$

where, $\emptyset_c^f$ is the critical porosity, which is assumed to be 0.98, and q is the power law exponent.

Based on Darcy's law, the following expression can be derived for the horizontal radial flow:

$$\dot{\mathrm{Q}} = \frac{\dot{m}}{\rho} = \frac{2\pi k_{i,j}^f a_{i,j} (P_{inj} - P_{res})}{\mu ln \frac{R_{max}}{R_0}} \tag{32}$$

where, R_{max} represents the radial distance where the maximum deposition rate localises. By coupling Eq. 1, 31, and 32, the goal of this entire model, the injectivity over time, can be computed.

3. MODELLING RESULTS AND DISSCUSION

As the domain is axis-symmetric, all results are shown in two-dimensional plots.

3.1 Hydrodynamic Conditions

The computed results suggest that Re is below 5 everywhere, so the flow is laminar in all locations throughout the 12-year injection. The effects of turbulent flow on particle transport and scale formation may be neglected and diffusion considered the dominant particle transport mechanisms.

3.2 Temperature distribution

The temperature distribution of the injected fluid along the fracture after 12 years of injection is shown in Figure 6.

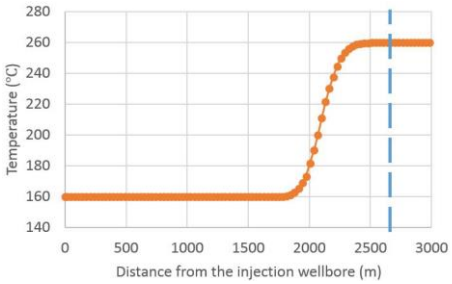

Figure 6: Injected fluid temperature vs. fluid spreading distance x. The dashed line represents the location of the injected fluid front.

There is an obvious temperature front around 2100 m, due to heat transfer from rock to fluid, forced convection, and diffusion. It is clear that the heat convection and diffusion (heat conduction within the fluid) happens between the injected and the reservoir fluids as soon as the reinjection starts. The dashed line is the fluid front, i.e. the boundary between the injected and pre-existing fluid, or the distance reached by the oldest injected fluid. If there is no mass or heat added to or removed from the injected fluid, all fronts (fluid, temperature, pH, and other chemical species) would be located at the same x. Heat transferred from the rock raises the oldest injected fluid to reservoir temperature, moving the temperature front closer to the wellbore. Diffusion smears the temperature distribution.

This heating increases the amorphous silica solubility at the very front of the injected fluid, affecting the silica polymerisation and the concentration of colloidal silica. This effect will be discussed further in Section 3.5.

3.3 pH distribution

The pH distribution of the injected fluid along the fracture is shown in Figure 7 below.

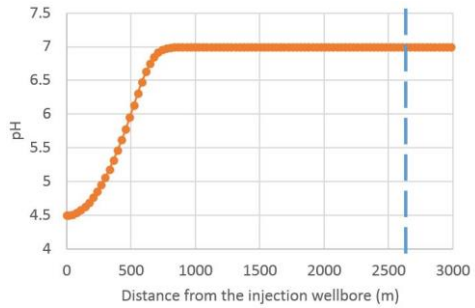

Figure 7: pH of injected fluid vs. fluid spreading distance x. The dashed line represents the location of the fluid front.

The pH front is affected by the dissolution of calcite in the pH<7 injected fluid, thus the pH front lags behind the injected fluid front. Brine acidification is employed as an effective method to inhibit silica scaling in the field as low pH inhibits silica nucleation. The present model shows the inhibiting effect decaying once the brines are injected into the reservoir and react with calcite.

3.4 Ionic strength distribution

A typical steam loss on flashing is between 20 - 30% depending on enthalpy. Excluding the gas content, the ionic strength of the injected fluid will be more than that of the reservoir fluid by the same amount. The ionic strength distribution is still required in the modelling to compute silica solubility and stability. The ionic strength (here equal to the concentration of sodium chloride) distribution along the fracture is shown in Fig. 8.

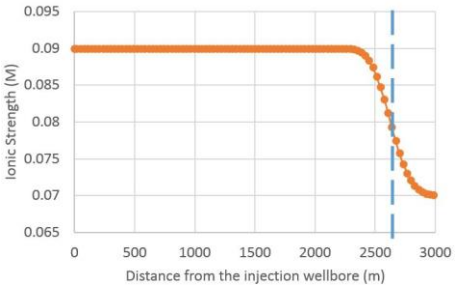

Figure 8: Ionic strength vs. fluid spreading distance x. The dash line represents the location of the fluid front.

The ionic strength and fluid fronts coincide, which is expected, since it is assumed that the sodium chloride in the injected fluid does not participate in any chemical reaction, i.e. neither generated nor destroyed.

3.5 Amorphous silica solubility and monomeric and polymerised silica concentration distribution

The temperature, pH, and ionic strength from the previous sub-models are used to estimate the solubility of amorphous silica (Figure 9).

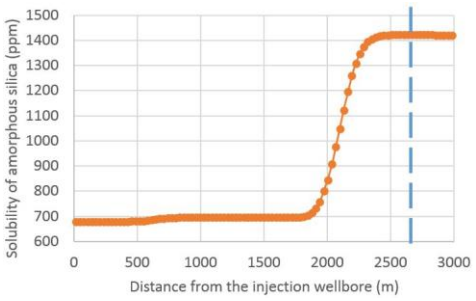

Figure 9: Amorphous silica solubility vs. fluid spreading distance x. The dashed line represents the location of the fluid front.

As the solubility is dominated by temperature, the curve is quite similar to the temperature distribution (Figure 6), and

the small rise around 700 m reveals the effect of calcite dissolution.

Weres et al. published a method to quantitatively predict the concentration decrement of dissolved silica due to silica polymerisation and homogenous nucleation under geothermal conditions, and noted it may be extrapolated up to 150℃. Here, the present model is validated against Weres' observations (not shown) and against Tobler and Benning's in-situ experiment (Figure 10).

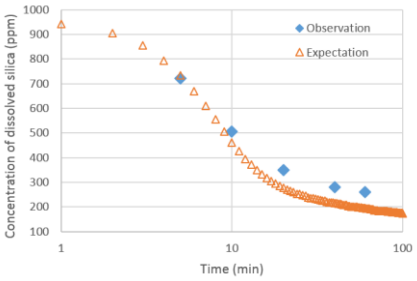

Figure 10: Comparison between predictions of the current model (triangles) and observations (diamonds) (reproduced from (Tobler and Benning 2013), pH = 7, I = 0.06 M, 303 K) and predictions (triangle dots).

Hence, the concentration decrement of dissolved silica in the case of geothermal reinjection can be reliably predicted with acceptable accuracy. The modelling results are shown in Figure 11.

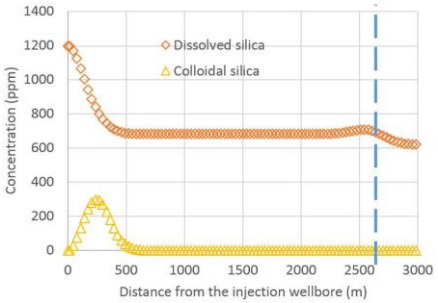

Figure 11: Dissolved (Diamond dots) and colloidal (Triangle dots) silica concentration distribution vs. fluid spreading distance x. The dashed line represents the location of the fluid front.

As shown in the figure above, along the fracture, the dissolved silica concentration drops rapidly from c_{inj}^{SiO2} due to polymerisation, nucleation, and molecular deposition, but rises again near the injected fluid front, and decreases to c_{res}^{SiO2} at the end due to mass convection and diffusion. All trends are expected but the concentration peak near the front should be noted. The reason for it is that the lag of the temperature front leads the silica saturation index near the fluid front to be relatively low, causing a correspondingly low polymerisation rate. This will affect the concentration of suspended colloidal silica and deposition rate.

3.6 Deposition rate

The deposition rate along the fracture is shown in Figure 12.

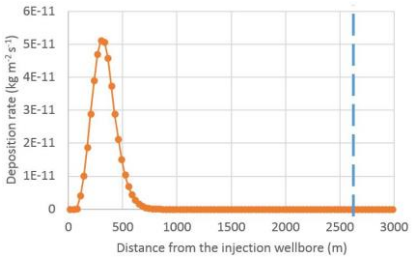

Figure 12: Amorphous silica deposition rate vs. fluid spreading distance x. The dashed line represents the location of the fluid front.

According to the modelling results, the maximum amorphous silica deposition rate is $\sim 10^{-11}\ kg(SiO_2)m^{-2}s^{-1}$, which is consistent with the observations ($10^{-10} - 10^{-11}\ kg(SiO_2)m^{-2}s^{-1}$) in the field (Wairakei, New Zealand) reported by (Carroll et al. 1998) under similar conditions. The empirical kinetic rate constant used in TOUGHREACT is of the same order of magnitude (Xu 2008).

If the porosity of silica scale is assumed to be zero, after 12 years' reinjection, the estimated thickness of the silica scale after 12-year reinjection is shown in Figure 13.

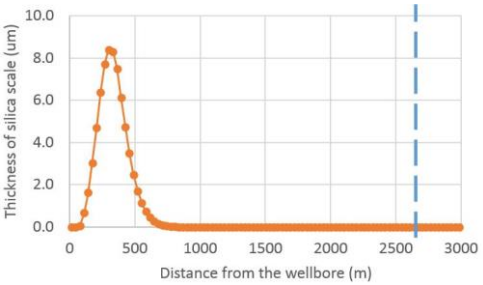

Figure 13: Localised silica scale thickness.

With the input values given above, the model predicts that the silica scaling is localised around 700m from the wellbore. This may be too far to allow chemical workover to be done efficiently. This location disagrees with observations at the Coso field (McLin et al. 2006), where deposition was found within 10 m of the wellbore. The chemical and flow conditions modelled above do not match the Coso field, and the current model assumes that only diffusion carries colloids to the wall. Inertial transport may be important where the fractures do not have straight, smooth walls. In addition, assumptions have been made about the silica and calcite chemistry and rate data has been extrapolated from observations at 300 K. These assumptions will be tested in future work.

The total volume of silica scale within one fracture is predicted to rise linearly after a slower period of approximately 0.5 years as shown in Figure 14.

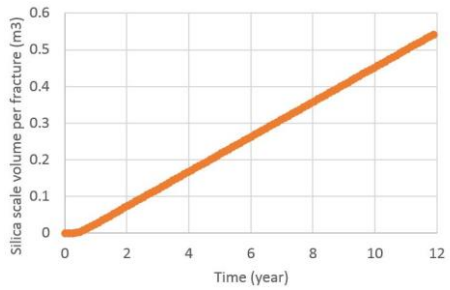

Figure 14: Volume of silica scale per fracture.

3.7 Injectivity

The computed injectivity as a function of time is shown in Figure 15:

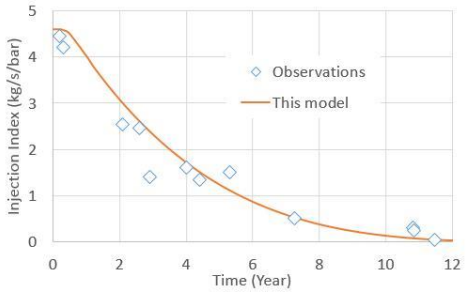

Figure 15: Expected injectivity curve after 12-year geothermal reinjection vs. observations reproduced from (Xu et al. 2004).

The injectivity curve shows a decline, at decreasing rate, in line with the modelling results of (Xu et al. 2004) . The discrepancy may be due to different reservoir geometries, e.g. fracture dimensions, permeable zone thickness etc. Note that for the same deposition rate, the injectivity drop will be slow when the aperture is millimetres wide, but rapid for micron level fractures.

4. CONCLUSIONS

A model of reinjection has been constructed, which includes sub-models of hydrodynamics, calcite chemistry, heat transfer, colloidal particle formation. Using observed stability data of silica colloids, the rate of deposition of amorphous silica is estimated. The predictions match field observations of injectivity drop reasonably well given the uncertainty in input data. Results depend on the validity of the assumptions, in particular the assumed stability of silica colloids, about which there remains some uncertainty. Future work will explore the effect of the assumptions and extrapolations used.

REFERENCES

Alexander, G. B. and J. R. McWhorter (1958). Concentrating silica sols without particle growth, Google Patents.

Arvidson, R. S., et al. (2003). "Variation in calcite dissolution rates: A fundamental problem?" Geochimica et cosmochimica acta 67(9): 1623-1634.

Carroll, S., et al. (1998). "Amorphous silica precipitation (60 to 120 C): Comparison of laboratory and field rates." Geochimica et cosmochimica acta 62(8): 1379-1396.

Derjaguin, B. V., & Landau, L. (1941). Theory of the stability of strongly charged lyophobic sols and of the adhesion of strongly charged particles in solutions of electrolytes. Acta physicochim. URSS, 14(6), 633-662. .

Elimelech, M., et al. (2013). Particle deposition and aggregation: measurement, modelling and simulation, Butterworth-Heinemann.

Frank-Kamenetskii, D. A. b. (1969). Diffusion and heat transfer in chemical kinetics, Plenum Press.

Keenan, J. H. (1969). Steam Tables; Thermodynamic Properties of Water Including Vapor, Liquid, and Solid Phases;-Metric Units, Wiley.

Leonard, B. P. (1979). "A stable and accurate convective modelling procedure based on quadratic upstream interpolation." Computer methods in applied mechanics and engineering 19(1): 59-98.

McLin, K. S., et al. (2006). Mineral characterization of scale deposits in injection wells; Coso and Salton Sea geothermal fields, CA. Thirty-First Workshop on Geothermal Reservoir Engineering, Stanford University, Stanford, California.

Nielsen, A. E. (1964). Kinetics of precipitation, Pergamon Press Oxford.

Plummer, L., et al. (1978). "The kinetics of calcite dissolution in CO 2-water systems at 5 degrees to 60 degrees C and 0.0 to 1.0 atm CO 2." American journal of science 278(2): 179-216.

Škvarla, J. i. (2013). "Quantitative interpretation of anomalous coagulation behavior of colloidal silica using a swellable polyelectrolyte gel model of electrical double layer." Langmuir 29(28): 8809-8824.

Tobler, D. J. and L. G. Benning (2013). "In situ and time resolved nucleation and growth of silica nanoparticles forming under simulated geothermal conditions." Geochimica et cosmochimica acta 114: 156-168.

Verma, A. and K. Pruess (1988). "Thermohydrological conditions and silica redistribution near high- level nuclear wastes emplaced in saturated geological formations." Journal of Geophysical Research: Solid Earth 93(B2): 1159-1173.

Verwey, E. J. W. and J. T. G. Overbeek (1955). "Theory of the stability of lyophobic colloids." Journal of Colloid Science 10(2): 224-225.

Wagner, C. (1961). "Ostwald ripening theory." Ber. Bunsenges. Phys. Chem 65: 581-591.

Weres, O., et al. (1981). "Kinetics of silica polymerization." Journal of Colloid and Interface Science 84(2): 379-402.

Wong, C., et al. (2016). Reactive transport modelling of injection fluid-reservoir rock interaction. New Zealand Geothermal Workshop 2016, Auckland, New Zealand.

Xu, T. (2008). "TOUGHREACT user's guide: A simulation program for non-isothermal multiphase reactive geochemical transport in variably saturated geologic media, V1. 2.1." Lawrence Berkeley National Laboratory.

Xu, T., et al. (2004). Reactive transport modeling of injection well scaling and acidizing at Tiwi field, Philippines. Geothermics, 33(4), 477-491.